Scilight

Journal of Bio-optics

https://www.sciltp.com/journals/jbo

Review

In-Vitro Methods for Comprehensive IOL Optical Performance Assessment

Dimitrios Christaras [1,*], Spyridon Tsoukalas [1], Alexandros Pennos [1], Harilaos Ginis [1] and Pablo Artal [2]

[1] Diestia Systems, 10441 Athens, Greece
[2] Laboratorio de Optica, Universidad de Murcia, 30100 Murcia, Spain
* Correspondence: dimitrios@diestia.com

How To Cite: Christaras, D.; Tsoukalas, S.; Pennos, A.; et al. In-Vitro Methods for Comprehensive IOL Optical Performance Assessment. *Journal of Bio-optics* **2025**, *1*(1), 5. https://doi.org/10.53941/jbiop.2025.100005.

Received: 19 May 2025
Revised: 19 August 2025
Accepted: 3 September 2025
Published: 11 September 2025

Abstract: This study introduces novel in-vitro methodologies for the optical assessment of intraocular lenses (IOLs), addressing the recognized gap between standard optical bench measurements and actual visual performance as experienced by patients. A model eye is presented that simulates the human eye's optical properties while allowing controlled measurements across various conditions. The testing framework incorporates three novel approaches: the High Dynamic Range Point Spread Function (HDR-PSF) method, which captures both fine central details and peripheral light scatter by combining multiple exposures, the Optical Integration Method, which quantifies straylight, and the Through-Focus Objective Letter Sharpness metric, which provides a visually relevant assessment of functional vision across different focal distances. Additionally, a systematic approach for evaluating negative dysphotopsia in the peripheral visual field is presented. These methodologies revealed significant differences in optical performance between various IOL designs, including monofocal, extended depth of focus and multifocal. The techniques provide deeper insights into IOL performance than current ISO and ANSI standards allow, offering more clinically relevant evaluations that better predict patient outcomes. This novel in-vitro testing framework represents an advancement in IOL evaluation, opening the way for improved lens design, better patient satisfaction, and more informed clinical decision-making in cataract surgery.

Keywords: intraocular lenses; in-vitro testing; cataract surgery; straylight; dysphotopsia

1. Introduction

Intraocular lenses (IOLs) have changed the treatment of cataract since their introduction by Harold Ridley in 1949, evolving significantly in both optical and mechanical design and materials [1]. The earliest IOLs were spherical and introduced substantial spherical aberration to the eye, [2] whereas modern aspheric lenses, now the most common type, were only introduced in the 2000s [3,4]. Recent advancements in IOL technology have focused on improving post-operative refractive accuracy and enhanced visual function, developing lenses that provide extended depth of focus or multiple foci, and enhancing peripheral vision [5,6].

Optical testing plays a crucial role in IOL manufacturing to ensure that each lens achieves its intended performance. Current standards such as ISO 11979-2 and ANSI Z80.35-2018 establish pass/fail criteria for quality control, typically requiring measurement of modulation transfer function (MTF) values at specific spatial frequencies in a through-focus manner [7,8]. However, these standard optical bench measurements often provide limited

information on the actual visual performance of IOLs in practical tasks, as the metrics used (such as MTF at specific spatial frequencies) do not directly correlate with patient-perceived visual quality in real-world conditions [9].

The diversity of IOL designs available today reflects various approaches to visual rehabilitation following cataract surgery. Monofocal IOLs, the most commonly used type, aim to provide optimal focus at a single distance, usually infinity (which in practice corresponds to viewing distances 3–6 m). Simultaneous vision IOLs often called multifocal IOLs and extended depth of focus (EDOF) IOLs are designed to reduce dependence on spectacles by providing either multiple foci or an extended focal range [5]. These lenses employ various diffractive and refractive designs to achieve different focal depths, reducing, however, image quality at various distances [10].

While patients generally achieve acceptable visual acuity with multifocal and EDOF lenses, clinical reports suggest that perceived image quality often fails to meet expectations, despite satisfactory acuity measurements [11]. This discrepancy indicates that improved in-vitro testing methods are needed to better predict how patients will actually see with different IOL designs in real-world conditions.

The gap between standard optical bench measurements and clinical outcomes creates a need for developing more sophisticated evaluation approaches. Recent research has explored visually relevant metrics for assessing IOL performance, including cross-correlation of blurred and original letter images [9], band-filtered optical transfer function metrics [12], and a cross-correlation metrics based on resolution charts [10]. These metrics aim to provide a more comprehensive understanding of how different IOL designs affect functional vision and quality of life outcomes.

One of the most important methods to assess optical performance of an optical system is the Point Spread Function (PSF). It represents one of the most fundamental metrics for characterizing optical systems, providing direct information about image quality by describing how a point source of light is distributed through the system. This metric reveals how well an optical system preserves spatial information, with a “perfect” system producing a perfect point and real systems showing various degrees of spreading. For optical systems like camera lenses or telescopes, measuring the PSF is relatively straightforward, but for the human eye—whether healthy or fitted with intraocular lenses (pseudophakic)—the measurement presents several challenges, related to the limited dynamic range of imaging sensors, but also other factors such as involuntary head movements, fundus diffusion phenomena, and eye pathologies. In the human eye, the PSF spans an extraordinarily wide dynamic range exceeding six orders of magnitude in intensity [13,14]. The central peak of the PSF, extending only about 0.02° of visual angle, is primarily affected by optical aberrations and directly correlates with visual acuity. Moving outward to approximately 0.33° corresponds to the domain assessed by contrast sensitivity tests. However, the peripheral zones beyond 1° from the center, which are predominantly associated with light scattering in the ocular media, have profound effects on vision quality despite their relatively low intensity. Increased straylight in these outer regions (from 1° to 100°) manifests as hazy vision, increased glare sensitivity, reduced contrast perception, and difficulties with face recognition in backlit conditions [14]. These visual disturbances can significantly affect quality of life, particularly in conditions such as cataract, corneal disturbances, or after refractive surgery, even when standard visual acuity measurements remain relatively preserved. This creates a challenging situation where conventional optical assessment methods fail to capture the complete picture. Traditional imaging sensors struggle with the extended dynamic range required, typically becoming limited by noise at relatively small angles around the PSF peak [13]. Consequently, the analysis of scattered light from double-pass images has historically been constrained to the central few tens of minutes of arc, leaving the wider-angle characteristics largely unmeasured by optical means. This limitation creates a diagnostic gap where patients may report significant visual disturbances despite having relatively good visual acuity measurements.

In this work we present a set of in-vitro tests, beyond the standard testing, developed in the lab to test the optical performance of IOLs. By bridging the gap between laboratory measurements and patient experience, the objective of this work is to inform manufacturers and physicians about the actual image quality in a through-focus manner as well as about the entoptic visual phenomena associated with IOL implantation such as dysphotopsias and glare. These testing methodologies may better predict visual outcomes and patient satisfaction, ultimately improving the matching of IOL designs to individual patient needs and expectations.

2. Methods

2.1. Model Eye

A model eye was developed for comprehensive optical assessment of intraocular lenses (IOLs) and other visual components. This physical eye model reproduces the optical properties and dimensions of the human eye, enabling precise through-focus analysis and visually relevant measurements of optical performance across the entire visual field.

The model consists of a custom-made meniscus lens acting as the cornea (EyeArt laboratories, Thessaloniki, Greece), with an anterior radius of curvature of 7.73 mm (conic constant −0.26) and a central thickness of 1 mm. The anterior surface closely resembles that of a human cornea in both base curvature and asphericity. The posterior curvature is specifically adjusted to compensate for the difference in refractive index between PMMA (n = 1.49 at 546 nm) and natural corneal tissue (n = 1.37 at 546 nm). This configuration produces a total corneal power of approximately 41.25 diopters and introduces +0.16 μm of spherical aberration (SA) for a 6 mm entrance pupil, matching human physiological values. Different PMMA corneas, with different anterior conic constants are available to model different amounts of corneal SA ranging from 0 to +0.28 μm. The measurements shown herein were made with the +0.16 μm cornea.

A key feature of this design is the exchangeable iris, allowing testing with different pupil sizes. In the standard configuration, a pupil diameter of 2.65 mm is used, corresponding to an entrance pupil of 3 mm in diameter. The iris is positioned at a depth of 3.6 mm from the anterior corneal surface. The IOL under investigation is suspended by its haptics in a dedicated receptacle positioned 4.1 mm from the anterior cornea, closely matching the anatomical position in human eyes after cataract surgery. The model eye also allows modifying the position of the IOL (through the exchange of the IOL holder) to simulate the various anterior chamber depth (ACD) values seen after cataract surgery and investigate in-vitro their effect in image quality. A schematic of the position of the IOL with respect to the cornea is shown in Figure 1.

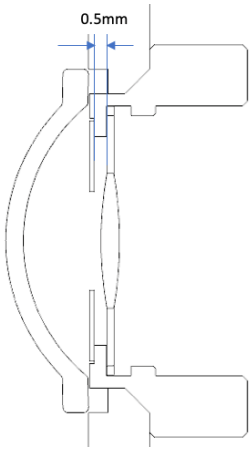

Figure 1. Nominal IOL position behind the iris (0.5 mm).

The imaging system utilizes a high-resolution CMOS camera housed in a water-tight container with its sensor in optical contact with a thin (200 μm) glass window via index matching adhesive. The space between the posterior corneal surface and the camera window is filled with pure water at room temperature (25 °C), creating a 23.4 mm axial length that closely simulates the aqueous and vitreous humors. Although the temperature of the eye model can be controlled to 37 °C by means of an external heater, the measurements shown in this work are typically performed in room temperature. The camera's pixel size of 2.2 μm results in a sampling frequency of 454.54 lines/mm at the retina plane, corresponding to 128.4 pixels/degree (for a 20D IOL), with a Nyquist frequency of 64.2 cycles per degree, equivalent to a visual acuity greater than 2.0 decimal (20/10).

The model eye retina/camera can be pivoted around an axis passing through the anatomical center of the retina (assuming a radius of curvature of 12 mm), allowing also peripheral vision assessment. This is especially valuable for studying optical phenomena such as off-axis astigmatism and field curvature that affect real-world visual performance but are often overlooked in standard optical bench testing. Additionally, the entire artificial eye is mounted on a rotating stage allowing a full 360-degree rotation with a step accuracy of 5 degrees, providing flexibility for evaluating optical performance across the entire visual field—a capability needed for assessing peripheral image quality and dysphotopic phenomena in pseudophakic eyes. Views of the model eye are shown in Figure 2.

All measurements using the model eye are conducted in a darkened laboratory environment with controlled ambient lighting (<1 lux). The measurement chamber was enclosed with blackout curtains to eliminate stray light, and all non-essential light sources such as monitors, indicating lights etc., were turned off during data acquisition. A custom 3D printed cap was used to cover the top of the model eye, blocking any straylight from reaching the sensor from the top opening.

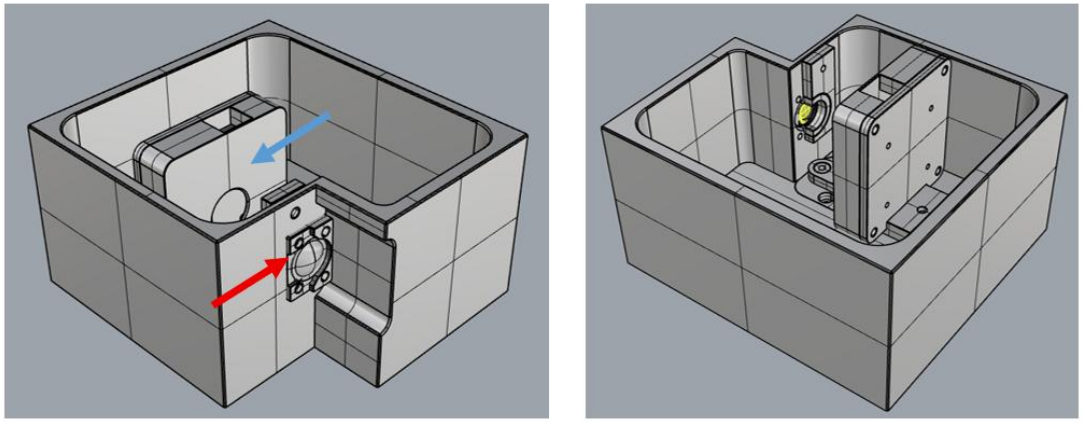

Figure 2. Two views of the model eye. In the left view the cornea is shown using the red arrow and the camera (acting retina) using a blue arrow. In the right view the IOL is shown in yellow. This whole assembly is filled with water.

2.2. Camera Calibration

The camera calibration procedure precisely characterizes the relationship between incident light intensity and camera response across the full dynamic range of the imaging system. Uniform discs of constant size were displayed on an external monitor but the ratio of white to black pixels within each disc varied. Beginning with a completely black disc (0% white pixels), we incrementally increase the white pixel ratio in steps (10%, 20%, 30%, and so on) until reaching a completely white disc (100% white pixels). In this process no imaging lens (or cornea) was used, but a small spacing of about 5 cm between the monitor and the camera's chip that ensures uniform illumination of the detector. The incident light on the detector is directly proportional to the number of "white" pixels, minus the contribution of the same number of "black" pixels. For each white pixel ratio, ten distinct random distributions of white pixels were generated within the disc. This randomization ensures that our measurements are not affected by any angular illumination artifacts or systematic spatial biases in the display or optical path. An example of three randomized discs at 30% and 70% white to black pixels is shown in Figure 3. The camera captures multiple frames for each of these patterns. The frames were then averaged to minimize random noise, calculating the mean intensity value from a central region of 3000 by 3000 pixels of the captured image.

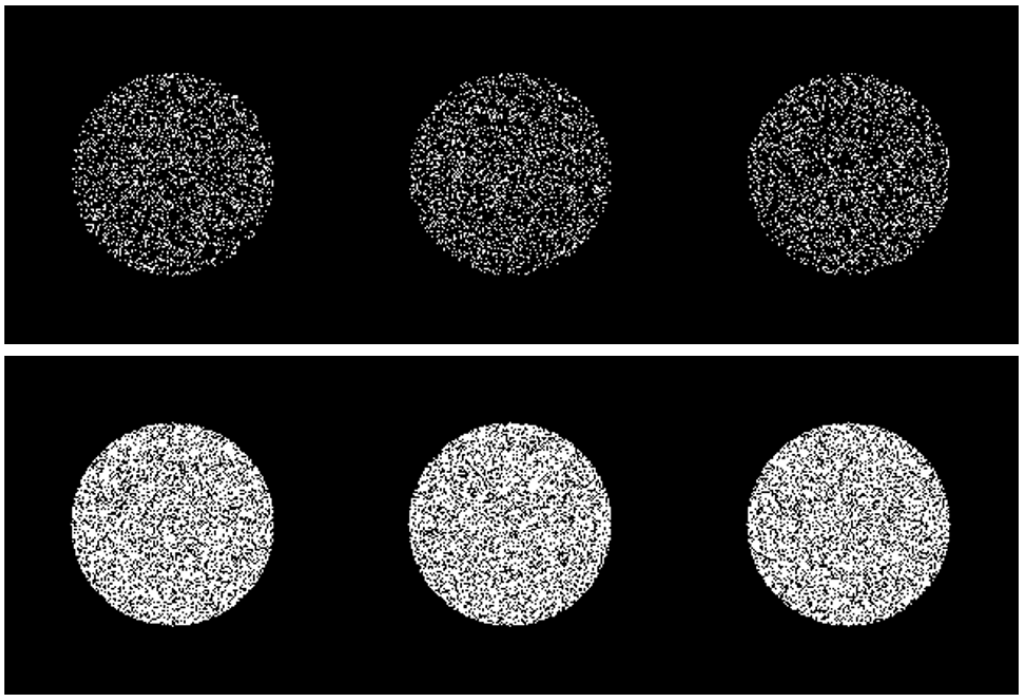

Figure 3. Example of white discs shown for the calibration of the camera at 20% of the total light (**top**) and 70% of the total light (**bottom**). Notice the difference in the white pixel location at each percentage (rows).

The calibration process produced a linear relationship between light intensity and camera response, accounting for dark current effects. The resulting calibration function converts raw camera counts to calibrated light intensity (for a single gain setting):

$$\text{Light} = \frac{1}{0.053818 \times \text{t}} \times \left(\text{cam} - (0.0026 \times \text{t} + 1.0768)\right)$$

where Light is the calibrated intensity (arbitrary units), cam is the detector response (counts), and t is the exposure time (ms). This function effectively linearizes the camera response across its full 12-bit dynamic range (0–4095 counts) and corrects for exposure-dependent dark current.

A critical aspect of calibration is the correction for the display's black level. Even pixels displayed as "black" emit a small amount of light, which can significantly affect measurements, especially at low intensities. This "black light" contribution per pixel was measured and subtracted from all measurements.

The total number of white pixels in each disc serves as the photometric reference value (arbitrary light units), providing an objective measure proportional to the total light flux. By collecting paired measurements of camera response versus white pixel count across the full range of intensities, a calibration function was developed that accurately maps camera response to actual light intensity throughout the system's dynamic range. The calibration process was carried out at several different exposure times and gain values of the camera. The produced calibration function was then applied to each image capture in the following IOL characterization methods resulting to pixel linearization.

2.3. HDR PSF Method

The need for measuring the complete PSF with high bit-depth, lead to the development of the High Dynamic Range Point Spread Function (HDR-PSF) assessment protocol. Designed for testing intraocular lenses in an artificial eye model, this method incorporates high dynamic range imaging techniques to capture the PSF across its full intensity range. By combining multiple exposures, the HDR-PSF method overcomes the dynamic range limitations of standard imaging sensors, enabling the accurate measurement of optical performance from the central peak to the faint peripheral scattered light. The HDR-PSF test provides a more comprehensive evaluation by quantifying light scatter across a wider field than previously possible. This approach allows a more complete picture of how optical imperfections affect vision under various lighting conditions, particularly in challenging scenarios such as night driving or backlit environments.

The technique uses a white arc lamp coupled to a 100 μm optical fiber as a point source stimulus at 4 m. Using the artificial eye model, multiple images of the resulting PSF were captured at different exposure times arranged in a geometric sequence. Typically, the process starts with a minimum exposure time (e.g., 4 ms), such that there are no saturated pixels in the image and the maximum intensity is just below saturation. For the 12-bit camera used this corresponds to 4095. This initial intensity is achieved by adjusting the arc lamp's intensity, depending on the transmittance of the IOL, the actual PSF and the pupil diameter. The exposure was then doubled for each subsequent capture (8 ms, 16 ms, 32 ms, and so on) until a sufficient exposure is reached, able to detect the faintest portions of the outskirts of the PSF. At each exposure setting, multiple frames were captured and averaged to improve the signal-to-noise ratio. To form the composite HDR image, each pixel is analyzed across all exposures and data from the exposure that provides adequate signal without saturation is selected. These values were normalized by their respective exposure times using the calibration function to maintain accurate relative intensity relationships. Custom MATLAB algorithms automatically exclude saturated pixels from the image with the highest exposure, using data from the next shorter exposure that remained unsaturated at those locations, until the shorter exposure is reached. This created a composite HDR image with no saturated pixels and information from short exposures, for the high-intensity central zone of the PSF, and long exposures, for the low-intensity peripheral zone of the PSF. In regions where multiple exposures provide usable data, a weighted blending approach was implemented to ensure smooth transitions between exposure zones.

Creating a 19-bit HDR image from a 12-bit camera illustrates the strength of this approach. A standard 12-bit camera provides 4096 discrete intensity levels (0–4095), with a baseline thermal noise of approximately 30 counts, yielding an effective dynamic range of only about 136:1 in a single exposure. By capturing eight exposure levels with times increasing by a factor of two (from 4 ms to 512 ms), the range increases from 12 to 19 bits, theoretically supporting over 500,000 distinct intensity levels. For a typical PSF measurement at the shortest exposure (4 ms), the central peak might register 4000 counts while a peripheral point at 3 degrees might record just 35 counts—barely above the noise floor. At the longest exposure (512 ms, 128 times longer), this same peripheral point would register approximately 4480 counts, providing excellent signal-to-noise ratio, while the central region would be completely saturated.

The resulting HDR-PSF spans the full six orders of magnitude required to characterize the complete optical performance of the eye, from fine central details affected by aberrations to the broad peripheral light distribution dominated by scatter.

The 2D image data is processed to extract a radial PSF profile. After centering at the peak intensity and averaging over multiple angles $\theta \in [-35°, 35°]$, the one-dimensional profile $\mathrm{PSF}(r)$ is obtained. This profile is normalized in two steps:

1. Radial weighting: To account for the 2D nature of the PSF, the profile was weighted by its radial coordinate:

$$\mathrm{PSF}_{\mathrm{integral}} = \int_{-r_{\max}}^{r_{\max}} \pi|r| \cdot \mathrm{PSF}(r)\, dr$$

2. Energy normalization: The profile is then normalized to unit energy:

$$\mathrm{PSF}_{\mathrm{normalized}}(r) = \frac{\mathrm{PSF}(r)}{\mathrm{PSF}_{\mathrm{integral}}}$$

For each optical system under test, the angular subtense per pixel was determined through a straightforward calibration process: An image of an object with known angular size (typically a 1-degree square) was captured at best focus, and the number of pixels spanning this object was measured. Dividing the known angular size by the pixel count gives the precise angular subtense per pixel. This calibration accounts for any magnification variations stemming from differences in lens power or position, ensuring accurate angular measurements regardless of the specific optical configuration.

As an example of this method, the HDR PSF of two distinct IOL lenses are shown in Figure 4: a monofocal and a multifocal (trifocal). For both IOLs best focus was achieved by maximizing the PSF at the shortest exposure time.

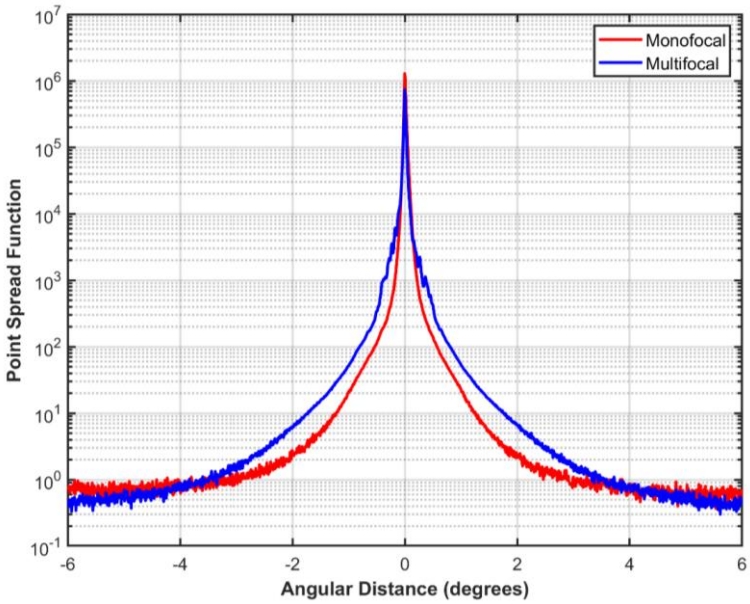

Figure 4. HDR PSF for two distinct IOLs, a conventional monofocal (20D) and a "premium" multifocal (20D) both at a pupil of 5 mm.

The resulting analysis allows the semi-quantitatively assessment of the quality of the PSF of two distinct IOLs with a pupil of 5 mm at best focus. In the example the multifocal IOL shows a lower peak and a wider distribution at lower angles; this would translate to reduced contrast sensitivity and slightly diminished visual acuity at the focal point compared to the monofocal IOL. Therefore, the monofocal lens, with its higher central peak and narrower distribution, would provide sharper vision and better contrast for distant objects at best focus. However, the multifocal's wider distribution reflects its design purpose of providing functional vision at multiple distances simultaneously, which necessarily comes at the expense of peak optical quality. The slightly lower background scatter observed in the multifocal at very high angles suggests potentially reduced glare sensitivity in low-light conditions when compared to the monofocal option, though this effect would be secondary to the more prominent differences in central vision quality and can be related with elevated straylight in a particular IOL due

to dirt. This method could allow us to in-vitro study the effects of glistenings, ageing even for the same lens and show differences between lens models related to their manufacturing process, handling etc.

2.4. Optical Integration Method

The optical integration method is a sophisticated approach for measuring indirectly the wide-angle Point Spread Function (PSF) in the presented model eye system. The method is based on the principle that the intensity at the center of a projected disc's image represents an integrated measurement of the optical system's PSF. When a uniform disc of radius θ is projected onto our model eye's sensor, the intensity at the center of the image, denoted as $I_c(\theta)$ is related to the PSF by:

$$I_c(\theta) = I_o \int_0^{\theta} 2\pi\phi \cdot PSF(\phi) d\phi$$

where I_o is the initial intensity. This integral equation can be differentiated to obtain:

$$PSF(\theta) = \frac{1}{2\pi\theta} \cdot \frac{dI_c^*(\theta)}{d\theta}$$

where $I_c^* = \frac{I_c}{I_o}$ represents the normalized intensity. Since the model eye employs a single-pass configuration with direct imaging of the object on the CMOS sensor, this PSF directly characterizes the optical properties of the tested components without the confounding factors of retinal reflection encountered in human eye measurements.

The implementation begins with a spatial calibration of the spatial relationship between the display and the model eye's optical system. For the specific system with a CMOS sensor of 2.2 μm pixel size and 128.4 pixels/degree resolution (with a 20D IOL), the conversion between pixels and visual angle is straightforward.

The measurement procedure involves projecting a series of uniform discs (Figure 5) with radii ranging from approximately 0.4 to 6 degrees onto the model eye's retina. The monitor pixels are converted to visual angle using:

$$a_{pixel} = \tan^{-1}\left(\frac{w/2}{d}\right) \cdot \frac{180}{\pi} \cdot \frac{1}{p/2}$$

where d represents the distance from the screen to the eye model (in mm), w is the physical width of the screen (in mm), and p is the screen resolution in pixels along the horizontal dimension. The formula converts the physical dimensions of the display setup to degrees of visual angle, providing the angular subtense of each pixel as viewed from the model eye.

Figure 5. Discs of increasing size projected sequentially onto the screen and captured by the model eye.

For each disc radius θ_i, multiple images are acquired to enhance signal-to-noise ratio. These images are averaged and corrected for camera dark current by subtracting a previously recorded dark frame:

$$I_{corrected}(\theta_i) = \frac{1}{n}\sum_{j=1}^{n} I_j(\theta_i) - I_{dark}$$

where n is the number of images (typically 10) acquired for each disc radius. The central intensity is extracted from each corrected image, yielding a dataset of intensity versus disc radius: $(\theta_i, I_c(\theta_i))$. Due to the sensitivity of numerical differentiation to noise, these data are fitted to a parametric model. A particularly effective model for our optical system is:

$$I_c^*(\theta) = \int_0^{\theta} \frac{A}{B + \phi^C} \cdot 2\pi\phi d\phi$$

where parameters A, B, and C are determined through nonlinear least-squares fitting. This approach provides robust PSF reconstruction even in the presence of measurement noise. To quantify the clinical relevance of measured scatter, the straylight parameter S was calculated, which has been introduced to characterize intraocular scatter. The straylight parameter S is calculated as:

$$S(\theta) = \theta^2 \cdot PSF(\theta)$$

For wide angles (typically 3–8 degrees), this parameter characterizes the overall scatter in the optical system. In our model eye, this parameter directly quantifies the scatter introduced by the IOL or other components under investigation. Furthermore, the optical integration method can be applied at multiple wavelengths to characterize the spectral dependence of scatter in various IOL materials, providing insights into the physical mechanisms responsible for light scatter (such as material inclusions, surface irregularities, or diffractive elements).

In the following example shown in Figure 6, this method was used to assess the severity of glistenings formed after incubation in vitro at 37 °C for different IOL materials that are under investigation (not clinical models). Figure 6a shows the glisterings of two different IOL models under the microscope. Figure 6b shows the normalized pixel intensity measured at the centre of each projected disc of different angular size (left) and the reconstructed PSF using the integration formula (right).

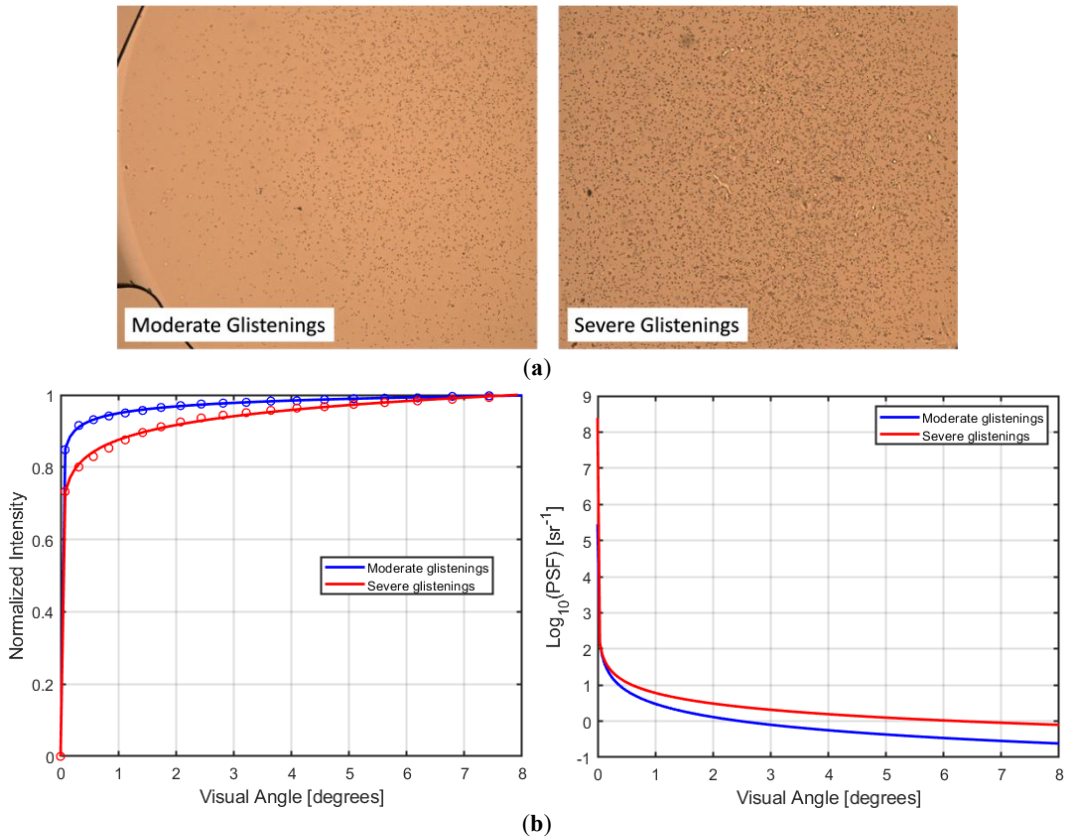

Figure 6. (**a**) Appearance of glistenings under the microscope; (**b**) Normalised intensity in the center of the discs (**left**) and reconstructed PSF (**right**) for a 3 mm aperture.

2.5. Through Focus Objective Letter Sharpness

This method involved recording through-focus images of standardized optotype charts through various intraocular lenses (IOLs) positioned using the model eye. The optical performance of each IOL was analyzed using an image quality metric, specifically designed to assess letter sharpness and contrast, to derive a visually relevant quantification of image degradation at different focal distances.

The experimental setup was built based on the model eye described earlier. A focus-tunable lens was incorporated into a 4f optical relay system to simulate different vergence conditions, allowing the assessment of through-focus performance. The tunable lens varied over a vergence range of approximately ±4 D in precise steps, ensuring the evaluation of the depth of focus for each IOL. A custom diaphragm wheel allowed for the selection of irises from 2 mm to 7 mm with a step of 0.5 mm. The optical system is seen in Figure 7. To mitigate the influence of system aberrations, lens centration and positioning were verified prior to each measurement using an auxiliary imaging setup.

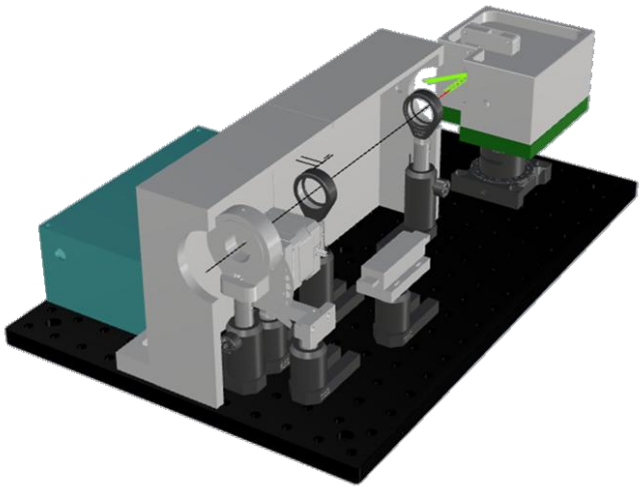

Figure 7. Optical setup featuring the artificial eye and a pupil conjugate tunable lens and adjustable pupil, allowing for the capturing of through focus images at different pupil sizes.

Optotype images were displayed on a computer monitor utilizing the green channel, which has a peak wavelength of approximately 548 nm, closely matching the standard photopic response of the human visual system. The displayed letter set consisted of Sloan optotypes, chosen for their well-balanced spatial frequency content. The letters were arranged in a three-line format, corresponding to different visual acuities, with the upper line set at a decimal visual acuity of 0.5 (20/40 Snellen equivalent), the middle line at 1.0 (20/20) and the lower at 0.25 (20/80). A sequence of captured images at different foci are shown in Figure 8.

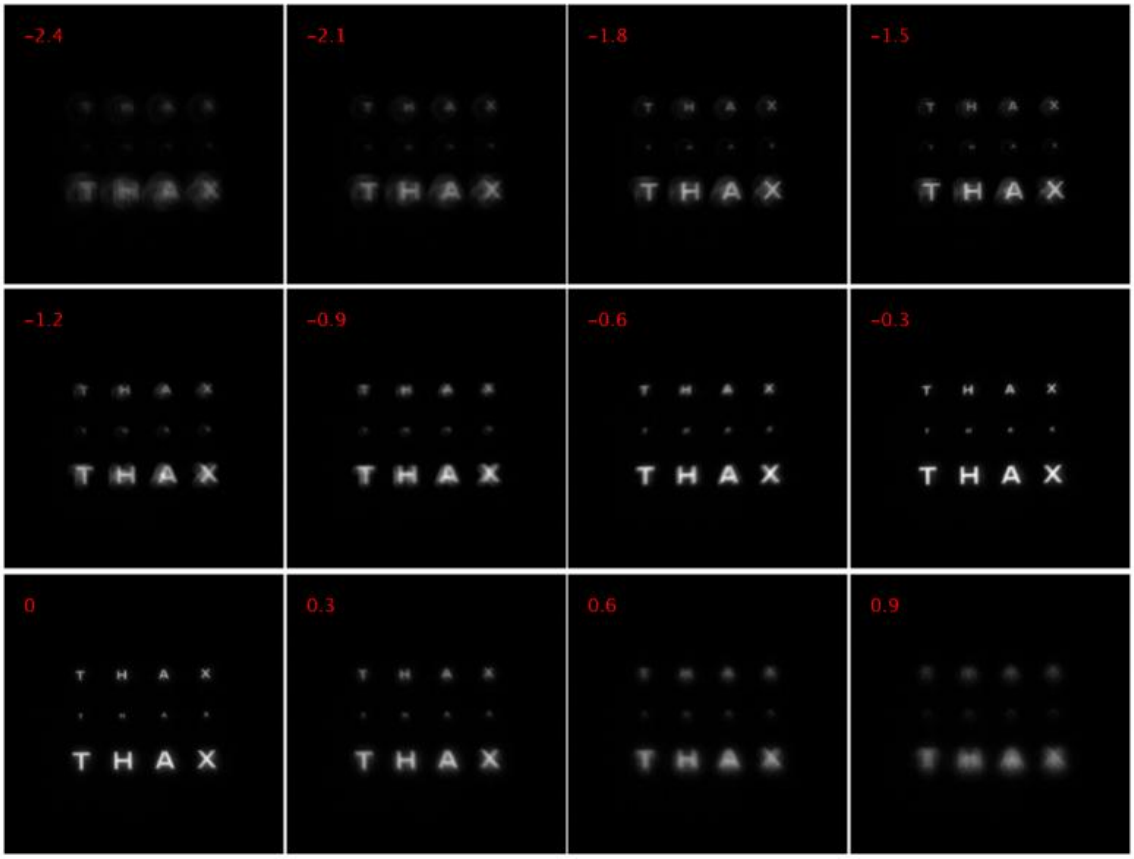

Figure 8. Through focus images of a sloan chart for a trifocal IOL. The letters in each image correspond to VA of 0.5 (**upper row**), 1.0 (**middle row**) and 0.25 (**lower row**) in decimal notation. In the top left corner of each image the focus is shown in diopters. In this example a pupil size of 4.5 mm.

A novel image quality metric, the Objective Letter Sharpness (OLS) parameter, was defined based on the normalized cross-correlation between the recorded and reference letter images. To emphasize visually relevant

features, both images were filtered in the Fourier domain using a band-pass function centered on the fundamental frequency of each letter. The OLS metric was computed as:

$$\mathrm{OLS} = \frac{\max\left[\mathcal{F}^{-1}\left((\mathcal{F}(\mathrm{I_o})\cdot \mathrm{M})\cdot\overline{(\mathcal{F}(\mathrm{I})\cdot \mathrm{M})}\right)\right]}{\sum|(\mathcal{F}(\mathrm{I_0})\cdot \mathrm{M}^2)|}$$

where I represents the recorded image, $\mathrm{I_0}$ the reference optotype, $\mathcal{F}$ denotes the Fourier transform, and M is a frequency-dependent band-pass filter. The fundamental frequency was scaled according to letter size, and the filter width was controlled to maintain relevant spatial information while suppressing noise contributions from higher-order harmonics.

Through-focus curves of OLS were obtained for each IOL by averaging the metric across multiple letters at each vergence step. A threshold OLS value of 0.1 was established empirically to define the practical depth of focus, corresponding to the dioptric range where optotype clarity remained functionally useful. Additionally, mean OLS values between distance vision and 50 cm were computed as an index of overall functional image quality, providing an objective measure of spectacle independence. Each lens was aligned and adjusted to its best focal position before recording through-focus sequences. To compensate for potential variations in nominal power or minor axial positioning errors, OLS curves were normalized by shifting their peaks to align with infinity focus conditions. As an example of this method, three different types of IOLs: a common monofocal, an EDOF and, finally, a bifocal, measured at 4.5 mm pupil are shown in Figure 9.

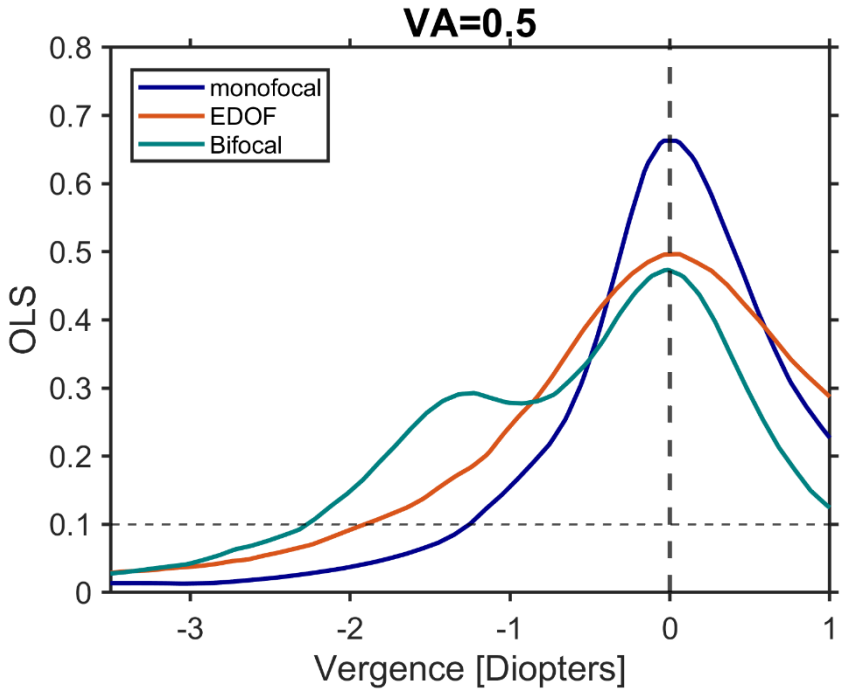

Figure 9. OLS for a monofocal, and EDOF and a bifocal IOL as a function of vergence in diopters. An empirical threshold of OLS = 0.1 was established as the lowest letter recognition threshold.

2.6. Peripheral Image Quality & Dysphotopic Phenomena

To objectively evaluate negative dysphotopsia (ND) in the far peripheral field, a systematic approach using the model eye was developed. This methodology allows for controlled comparison of different IOL designs under standardized conditions.

The experimental setup, seen in Figure 10a, consists of the model eye positioned at a fixed distance from a high-resolution LCD display. This display serves as an extended light source, projecting a horizontal luminous bar (5° vertical × 15° horizontal) at the far peripheral visual field (roughly 70° to 85° from the visual axis). The position and dimensions of this bar are controlled through custom software, allowing for reproducible stimulation of the eye's far periphery, as shown in the schematic in Figure 10b. The system allows also the use of a point source at the location of the monitor. This configuration allows the reconstruction of the peripheral PSF. In order to capture the peripheral PSF the whole model eye is rotated on its mount and the camera is then pivoted to bring the point source at the centre of its field.

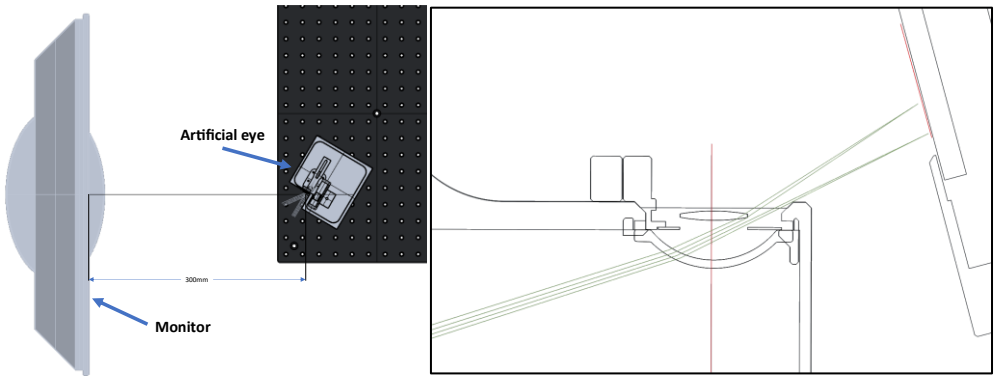

(**a**) (**b**)

Figure 10. (**a**) Setup to evaluate dysphotopic phenomena in the peripheral field. (**b**) Schematic indicating some rays missing the edge of the IOL and arriving at a different location on the detector.

For each test condition, ten consecutive frames were acquired which were subsequently averaged to improve signal-to-noise ratio. A dark frame, captured with the display turned off, is subtracted from each averaged image to eliminate camera noise and stray light within the system. In order to be able to compare different lens models for dysphotopic phenomena, it is important to ensure that the IOLs and the iris are perfectly aligned, as empirical data show that small misalignments can have a big impact on dysphotopsias. Alignment was done with the help of a second CMOS camera focusing on the iris plane of the model eye and a MATLAB script which automatically detects the iris and the IOL. This allows us to perfectly align the IOLs and the irises and maintain almost identical conditions between measurements. An example is shown in Figure 11a.

The model eye allows for different anterior chamber depths (ACD) to be explored. This is done by using appropriate mounts with the desired spacing, as seen in Figure 11b.

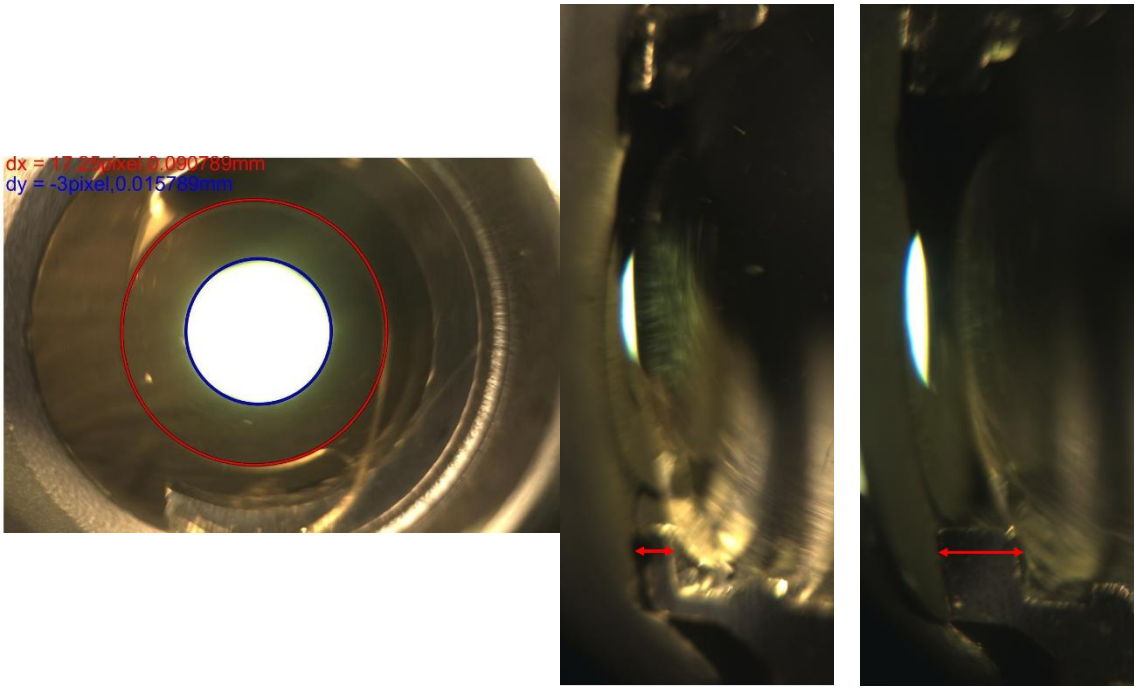

(**a**) (**b**)

Figure 11. (**a**) Alignment of the IOL. The red circle depicts the limits of the IOL and the blue the limits of iris (in this example 3 mm); (**b**) Two different mounts for the IOL resulting to two distinct ACDs (0.5 mm and 1.5 mm), allowing us to explore the relation between the position of the IOL and the presence of photopic phenomena. A side-view camera allows the confirmation of proper seating of the IOL's haptics against the desired reference plane.

For quantitative analysis of the captured images, horizontal intensity profiles across the region of interest were extracted where the shadow phenomena were expected to occur. These intensity profiles are plotted against visual angle, allowing for precise localization and characterization of any shadow artifacts. The shadow's intensity, width, and position are quantified through the analysis of these profiles. Furthermore, a qualitative analysis is

performed, by examining the distribution of the peripheral PSF. An example of a peripheral PSF image at 45 degrees, with a pupil of 3 mm and a distance from the iris of 1.5 mm is shown in Figure 12. As seen in Figure 12, the characteristic crescent from the light missing the IOL's edge can appear in field angles as low as 45 degrees. It is not until much wider angles that this phenomenon leads to the formation of "shadows". This occurs at those angles (typically around 75° where the light propagated through the IOL is completely vignetted while the light propagating around the edge of the IOL persists, as seen in Figure 13.

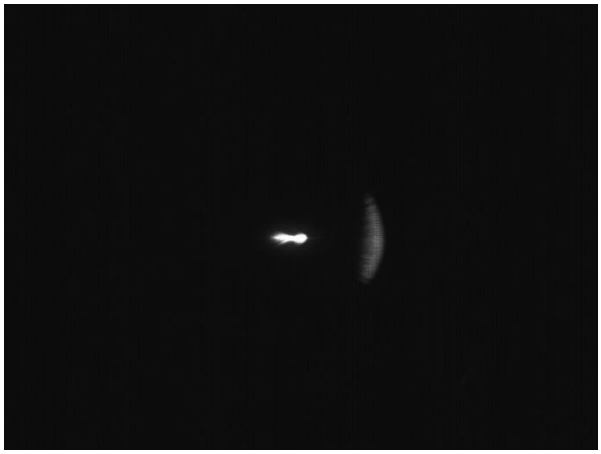

Figure 12. Peripheral PSF at 45 degrees using an iris of 3 mm and a distance between the IOL and the iris of 1.5 mm.

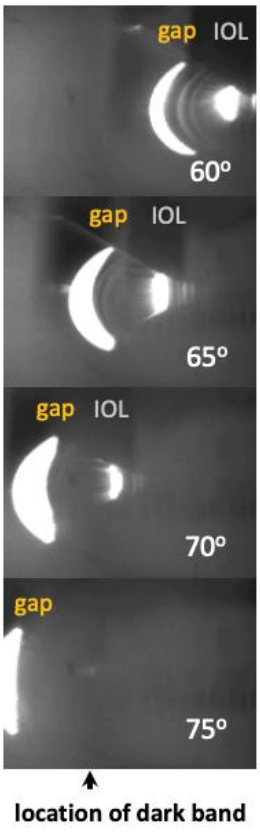

Figure 13. Spatial dependence of the PSF showing the transition from IOL-transmitted light (top) to edge-diffracted light (right). At approximately 75° (depending on pupil diameter and anterior chamber depth), IOL-transmitted light becomes completely vignetted while edge-scattered light persists, creating the characteristic shadow band associated with dysphotopsia.

Figure 14 shows example images of the horizontal bar with 2 different types of IOLs one having the shape of an inverted meniscus and one standard biconvex.

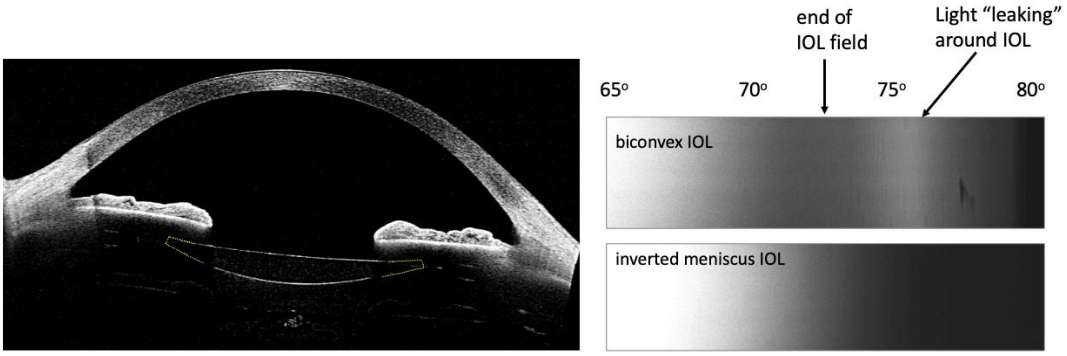

Figure 14. Left: OCT image of an inverted meniscus IOL (separate clinical image for illustration). Right: Schematic cross-section of the model eye showing the narrower gap between the IOL edge and posterior iris surface, which reduces light bypass around the IOL edge.

For quantitative analysis, such images are analyzed further by applying the calibration function using the specific exposure time for each IOL as described earlier. After calibration, the mean intensity value across all rows was calculated for each remaining column position, producing a one-dimensional profile that represents the average intensity distribution across the image. This profile is then mapped to visual field coordinates spanning from 70 to 85 degrees, allowing direct comparison of how light intensity varies across the visual field for each IOL design. The resulting plot displays these mean intensity profiles as continuous lines, allowing a direct assessment of the dysphotopic phenomena in the far periphery, as shown in Figure 15.

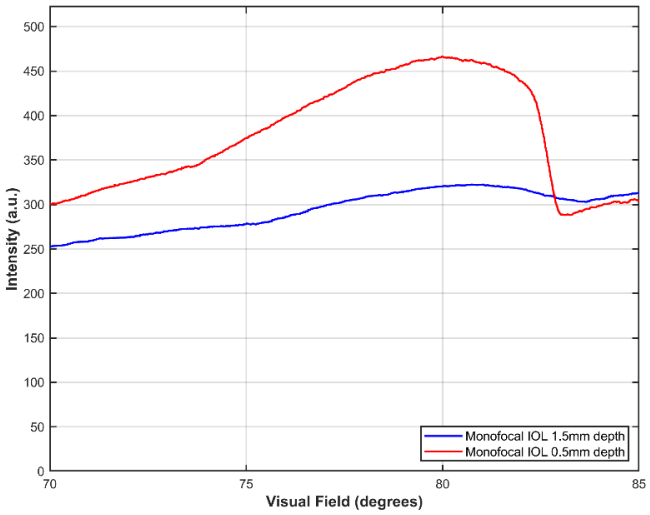

Figure 15. Profile plots for a biconvex monofocal IOL with 3 mm pupil at two different anterior chamber depths (0.5 mm and 1.5 mm posterior to iris plane).

3. Discussion

A set of in-vitro testing methodologies are presented in this study, aiming to bridge a known gap between standard optical bench measurements and the actual visual performance of intraocular lenses (IOLs) in clinical settings.

The HDR-PSF method overcomes the limited dynamic range of conventional sensors by combining multiple exposures, enabling the quantification of both central and peripheral PSF, critical for assessing glare. Similarly, the Optical Integration Method provides a robust way to isolate IOL-induced straylight and has the potential to detect the smallest changes in media transparency. The OLS metric, derived from cross-correlation analysis of Sloan optotypes, offers a clinically relevant measure of functional vision, showing both in a qualitative and quantitative way the visual performance of an IOL at different foci.

The proposed metrics offer several advantages over conventional IOL assessment methods currently specified in ISO 11979-2 and ANSI Z80.35-2018 standards. Traditional MTF measurements at discrete spatial frequencies (e.g., 25, 50, and 100 cycles/mm) provide limited insight into functional vision, as they do not account

for the visual system's spatial frequency response or real-world viewing tasks. In contrast, the HDR-PSF method captures the complete optical transfer function across six orders of magnitude, revealing both high-frequency detail preservation and wide-angle scatter characteristics that directly correlate with glare sensitivity and contrast perception under different lighting conditions. The Optical Integration Method provides quantitative straylight assessment that complements but differs fundamentally from conventional double-pass PSF measurements used in clinical instruments. The Through-Focus Objective Letter Sharpness (OLS) metric differs from traditional MTF-based assessments by incorporating visually relevant spatial frequency content and letter recognition tasks. Unlike single frequency MTF, area-under-the-MTF curves or Strehl ratios that focus only on a single MTF value or weight all spatial frequencies equally, OLS emphasizes frequencies crucial for optotype recognition, providing better correlation with functional visual acuity, allowing the visual assessment of both monofocal and multifocal and EDOF IOLs.

A full assessment of straylight phenomena requires understanding the multiple parameters that influence these measurements—factors that advanced methodologies are specifically designed to capture and control. Research has demonstrated that straylight in the human eye exhibits wavelength dependence, with significant variations across the visible spectrum. Ginis et al. showed that small angle straylight is strongly influenced by wavelength, particularly beyond 600 nm where fundus reflectance contributes substantially to the total straylight [15]. Christaras et al. further clarified this relationship using Monte Carlo simulations, establishing that fundus-scattered light's spatial contribution is limited to narrower angles (up to 2° at 560 nm and 4–4.5° at 650 nm) compared to light scattered in the ocular media, which extends to wider angles with less wavelength dependence [16]. Additionally, ocular biometry—particularly axial length, has been shown to affect straylight measurements. Christaras et al. demonstrated that in myopic eyes corrected with spectacles, the eye's second nodal point shifts toward the retina, resulting in increased perceived straylight [17]. Testing frameworks must account for the key factors affecting measurement outcomes. Pupil size affects all three metrics, with smaller apertures (2–3 mm) revealing central optical quality while larger pupils (5–6 mm) expose multifocal zone interactions and peripheral dysphotopic phenomena. Anterior chamber depth (ACD) variations significantly influence dysphotopsia occurrence, as IOL positioning relative to the iris affects light propagation around the lens edge. Illumination conditions impact straylight measurements, particularly relevant for HDR-PSF methods under mesopic conditions. IOL design interactions vary significantly, with diffractive multifocals showing characteristic multi-peak through-focus curves while refractive designs exhibit smoother through-focus transitions.

These parametric dependencies highlight why conventional standards like ISO 11979-2 and ANSI Z80.35-2018 often fail to capture the full spectrum of visual phenomena, such as straylight, peripheral dysphotopsia, and functional vision across varying distances, as they do not account for the complex interactions between these multiple factors.

While the presented methodologies focus on monocular retinal image quality assessment, real vision is mostly binocular, and real-world visual performance depends on the combination of images from both eyes. The visual system employs sophisticated mechanisms to optimize binocular vision, including suppression, summation, and interocular competition, particularly when asymmetric optical quality exists between the two eyes [18,19]—as commonly occurs with monovision correction [20] or different IOL designs in each eye [21]. Future extensions of these methodologies should incorporate binocular assessment, potentially through dual model eye systems that simulate binocular integration. Such developments would be particularly valuable for evaluating presbyopia-correcting IOL strategies and would significantly enhance the clinical relevance of this testing framework.

Furthermore, the current testing framework is optimized for eyes with normal optical properties, representing the majority of cataract surgery candidates. However, a significant subset of patients undergoing IOL implantation present with irregular corneal optics, including those with keratoconus, post-refractive surgery corneas, or significant higher-order aberrations. The optical performance of IOLs in such eyes may differ substantially from that predicted by standard testing conditions, as the interaction between corneal irregularities and IOL optics can produce complex aberration outcomes [22–24]. Future developments should incorporate variable corneal models that simulate different degrees of corneal irregularity, and the metrics may require optimization when applied to eyes with irregular optics, as the relative importance of optical quality parameters may change in the presence of pre-existing aberrations.

Also, it needs to be noted here that the letter spacing in the optotype charts was optimized for the imaging system's resolution but may be larger than standard clinical charts. This could potentially reduce crowding effects and should be considered when translating results to clinical visual acuity predictions.

Other limitations must be acknowledged too. While the model eye closely mimics human ocular anatomy, naturally, it cannot fully replicate biological variability, such as individual differences in corneal asphericity and neuroadaptation [25]. The HDR-PSF method, though powerful, requires meticulous calibration and multiple

exposures, which may limit its practicality for high-throughput manufacturing quality control. The OLS metric, while effective, depends on specific optotype designs and filtering parameters, potentially restricting its generalizability. Dysphotopsia assessment is prone to alignment errors and is constrained by the fixed geometry of the model eye.

Future research should focus on refining these methodologies for broader clinical and industrial adoption. Incorporating patient-specific anatomical data into the model eye could improve its predictive accuracy, while automation of the HDR-PSF and Optical Integration methods could enhance their feasibility for routine testing. Expanding the OLS metric to include a wider range of optotypes and spatial frequencies would further strengthen its clinical relevance.

In conclusion, this novel in-vitro testing framework provides a significant leap forward in IOL evaluation, offering deeper insights into optical performance and functional vision. By addressing the shortcomings of current standards and incorporating visually meaningful metrics, these methods pave the way for improved IOL design, better patient outcomes, and more informed clinical decision-making.

Author Contributions

D.C.: conceptualization, methodology, software, validation, investigation, visualization, writing—original draft preparation; S.T.: validation, investigation, visualization, writing—reviewing and editing; A.P.: conceptualization, methodology, writing—reviewing and editing; H.G.: conceptualization, methodology, software, validation, writing—reviewing and editing; P.A.: conceptualization, methodology, writing—reviewing and editing, supervision. All authors have read and agreed to the published version of the manuscript.

Funding

This research was funded by Velux Stiftung, Switzerland, project number 1385 and co−financed by the European Regional Development Fund of the European Union and Greek national funds through the Operational Program Competitiveness, Entrepreneurship and Innovation, under the call RESEARCH−CREATE−INNOVATE (project code: TAEDK−06187).

Conflicts of Interest

The authors have no conflict of interest to declare.

References

1. Apple, D.J.; Sims, J. Harold Ridley and the invention of the intraocular lens. *Surv. Ophthalmol.* **1996**, *40*, 279–292.
2. Guirao, A.; Redondo, M.; Geraghty, E.; et al. Corneal optical aberrations and retinal image quality in patients in whom monofocal intraocular lenses were implanted. *Arch. Ophthalmol.* **2002**, *120*, 1143–1151.
3. Tabernero, J.; Piers, P.; Benito, A.; et al. Predicting the optical performance of eyes implanted with IOLs to correct spherical aberration. *Investig. Ophthalmol. Vis. Sci.* **2006**, *47*, 4651–4658.
4. Artal, P. History of IOLs that correct spherical aberration. *J. Cataract Refract. Surg.* **2009**, *35*, 962–963.
5. Rampat, R.; Gatinel, D. Multifocal and extended depth-of-focus intraocular lenses in 2020. *Ophthalmology* **2021**, *128*, e164–e185.
6. Artal, P.; Ginis, H.; Christaras, D.; et al. Inverted meniscus intraocular lens as a better optical surrogate of the crystalline lens. *Biomed. Opt. Express* **2023**, *14*, 2129–2137.
7. International Organization for Standardization ISO Central Secretariat. *International Standard ISO 11979-2: Ophthalmic Implants—Intraocular Lenses, Part 2: Optical Properties and Testing Procedures*; ISO: Geneva, Switzerland, 2014.
8. American National Standards Institute. *ANSI Z80.35-2018: Ophthalmics—Extended Depth of Focus Intraocular Lenses*; American National Standards Institute: Washington, DC, USA, 2018.
9. Ginis, H.S.; Tsoukalas, S.; Christaras, D.; et al. Visually relevant on-bench through-focus analysis of intraocular lenses. *Biomed. Opt. Express* **2024**, *15*, 7056–7065.
10. Alarcon, A.; Canovas, C.; Rosen, R.; et al. Preclinical metrics to predict through-focus visual acuity for pseudophakic patients. *Biomed. Opt. Express* **2016**, *7*, 1877–1888.
11. Arias, A.; Ginis, H.; Artal, P. Straylight in different types of intraocular lenses. *Transl. Vis. Sci. Technol.* **2020**, *9*, 16.
12. Ravikumar, A.; Marsack, J.D.; Bedell, H.E.; et al. Change in visual acuity is well correlated with change in image-quality metrics for both normal and keratoconic wavefront errors. *J. Vis.* **2013**, *13*, 28.
13. Ginis, H.; Pérez, G.M.; Bueno, J.M.; et al. The wide-angle point spread function of the human eye reconstructed by a new optical method. *J. Vis.* **2012**, *12*, 20.

14. van den Berg, T.J.; Franssen, L.; Coppens, J.E. Straylight in the human eye: Testing objectivity and optical character of the psychophysical measurement. *Ophthalmic Physiol. Opt.* **2010**, *30*, 345–350.
15. Ginis, H.; Perez, G.M.; Bueno, J.M.; et al. Wavelength dependence of the ocular straylight. *Investog. Ophthalmol. Vis. Sci.* **2013**, *54*, 3702–3708.
16. Christaras, D.; Ginis, H.; Pennos, A.; et al. Scattering contribution to the double-pass PSF using Monte Carlo simulations. *Ophthalmic Physiol. Opt.* **2017**, *37*, 342–346.
17. Christaras, D.; Rozema, J.J.; Ginis, H. Ocular axial length and straylight. *Ophthalmic Physiol. Opt.* **2023**, 40, 316–322.
18. Stidwill, D.; Fletcher, R. *Normal Binocular Vision: Theory, Investigation and Practical Aspects*, 1st ed.; Blackwell Publishing: Hoboken, NJ, USA, 2011.
19. Radhakrishnan, A.; Dorronsoro, C.; Sawides, L.; et al. A cyclopean neural mechanism compensating for optical differences between the eyes. *Curr. Biol.* **2015**, *25*, 188–189.
20. Evans, B.J.W. Monovision: A review. *Ophthalmic Physiol. Opt.* **2007**, *27*, 417–439.
21. Kim, B.; Son, H.S.; Khoramnia, R.; et al. Comparison of clinical outcomes between different combinations of hybrid multifocal, extended-depth-of-focus and enhanced monofocal intraocular lenses. *Br. J. Ophthalmol.* **2025**, *109*, 565–571.
22. Park, D.Y.; Lim, D.H.; Chung, T.Y.; et al. Intraocular lens power calculations in a patient with posterior keratoconus. *Cornea* **2013**, *32*, 708–711.
23. Zhang, M.; Qian, D.; Jing, Q.; et al. Analysis of Corneal Spherical Aberrations in Cataract Patients with High Myopia. *Sci. Rep.* **2019**, *9*, 1420.
24. Yoo, Y.S.; Kang, M.C.; Park, J.; et al. Factors affecting prediction error after cataract surgery with implantation of various multifocal IOLs in patients with previous refractive laser surgery. *Ann. Transl. Med.* **2021**, *9*, 1720.
25. Zhang, L.; Lin, D.; Wang, Y.; et al. Comparison of Visual Neuroadaptations After Multifocal and Monofocal Intraocular Lens Implantation. *Front. Neurosci.* **2021**, *15*, 648863.